Journal of Nanophotonics

SPIEDigitalLibrary.org/jnp

Detailed study of surface-enhanced Raman scattering from metallic nanosculptured thin films and their potential for biosensing

Atef Shalabney
Chinmay Khare
Jens Bauer
Bernd Rauschenbach
I. Abdulhalim

SPIE

Detailed study of surface-enhanced Raman scattering from metallic nanosculptured thin films and their potential for biosensing

Atef Shalabney,[a] Chinmay Khare,[b] Jens Bauer,[b] Bernd Rauschenbach,[b,c] and I. Abdulhalim[a,d]

[a]Ben Gurion University, Department of Electro optic Engineering and The Ilse Katz Institute for Nanoscale Sciences and Technology, Beer Sheva 84105, Israel
shalaban@bgu.ac.il

[b]Leibniz-Institute of Surface Modification, Permoserstrasse 15, 04318 Leipzig, Germany

[c]University Leipzig, Institute for Experimental Physics II, Linnéstr. 5, 04307 Leipzig, Germany

[d]Nanyang Technological University, School of Materials Science and Engineering, 637722, Singapore

Abstract. Surface-enhanced Raman scattering (SERS) from silver nanosculptured thin films (STF) was studied in detail for biosensing. The influences of the nanostructures' sizes, topology, the substrate features, and the preparation conditions on the enhancement were examined. Enhancement factors on the order of 10^7 were obtained from silver nanorods deposited on bare silicon substrates with respect to their dense counterparts, using 4-aminotheophenol (4-ATP) for the Raman emission. The low detection limit that can be achieved with STFs is below 1 μg/lit of the probe molecule 4-ATP in Ethanol solution. Theoretical modeling based on a single small spheroidal nanoparticle helped in explaining the main properties of SERS from STFs. Stability of the films was noticed over a period of one year without significant degradation. [DOI: 10.1117/1.JNP.6.061605]

Keywords: glancing angle deposition; surface-enhanced Raman scattering; Raman enhancement factor; sculptured thin films.

Paper 12027SS received Mar. 28, 2012; revised manuscript received May 29, 2012; accepted for publication Jul. 24, 2012; published online Sep. 18, 2012.

1 Introduction

Surface enhanced Raman scattering (SERS) technique has a great potential for variety of environmental or medical sensing applications as it can afford small limits of detection and specificity. Several mechanisms of enhancement were proposed in the early days of SERS investigations[1,2] to account for the experimental facts observed. These mechanisms converged with the years into two classes, which were called the electromagnetic mechanism (EM) and the chemical mechanism (CM).[2] The EM mechanism is caused by the nanoscale roughness of the surface under consideration. The key result is that surface plasmons can be excited, resulting in an enhanced electromagnetic field close to the surface. In Raman scattering, the intensity depends on the square of the incident field strength; as a result, the intensity will be enhanced relative to what it would be in the absence of the surface. The Raman emitted field may also be enhanced, generally by a different amount than the incident field, because the frequency is different. The overall enhancement associated with the incident and the emitted field enhancement is called the EM contribution to SERS (see Appendix). The CM of enhancement comes, in particular, to explain the difference between the intensities obtained from different molecules despite the fact that they have the same polarizability.

In the last decade, a tremendous progress was achieved in fabricating variety of nanostructures and nanoparticles that support localized surface plasmon resonances (LSPRs) in the visible

0091-3286/2012/$25.00 © 2012 SPIE

and the UV range. Plasmonic effects appear at the interfaces between metals and dielectrics and include variety of phenomena such as enhanced transmission through nanoholes,[3] field enhancement and with it enhanced spectroscopies[4–8] and other properties such as enhancing the efficiency of solar cells.[9] One of the most attractive features of the EM mechanism is that the enhancement and its wavelength dependence can be estimated by calculations that require only the size, shape, and the dielectric function of these nanostructures. A number of calculations of the enhancement based on this idea appeared in the literature. Kerker et al.[10] developed a theoretical model for a molecule on or near a spherical particle. Also Ohtaka[11] did the same derivation for two spheres using more complicated rigorous calculations. Moskovits[12] summarized through a comprehensive review study, calculations for spheroidal nanoparticles and several methods of treating the case of roughened surface that will be considered in our discussion. Shrader and Moore[13] surveyed the physics of Raman spectroscopy and the relevant instrumentation. More updated work was done by Schatz and Van Duyne[14] in which they expanded the discussion to various particle shapes and materials with graphic results that may be useful for multi particle system analysis.

Since SERS is a powerful analytical tool for obtaining vibrational information for molecules, and since this signal can be considerably enhanced by metallic nanoparticles, many works were done in the field of biosensing using a wide variety of engineered nanostructures, including the detection of single molecules.[15] Orendroff and coworkers[16] examined the effect of the aspect ratio of silver and gold separated nanorods on SERS enhancement. They found that silver and gold nanorods with aspect ratio of 10 and 1.7, respectively, give the largest enhancement factors. Raman difference spectroscopy (RDS) was used by Lee et al.[17] to investigate the physical aging phenomenon of the molecule Bisphenol-A—polycarbonate (BPAPC). Nicrosis due to chemotherapy and radiotherapy in treating tumors was detected by SERS spectroscopy,[18] glycated hemoglobin (HbA1c) in diabetics,[19] detecting viruses,[20] and single molecule spectroscopy (SMS) of hemoglobin (Hb) by silver nanoparticles was examined.[21] Structures of the form of dielectric-metallic core-shell,[22] flowerlike nanoparticle arrays, nanoflowers, nanowires networks, nanosheets,[23] and the combination substrate-molecule-silver (gold) nanoplates[24] also were investigated for SERS enhancement.

Localized surface plasmon (LSP) from an array of particles deposited on a substrate differ from the LSP on the surface of a single particle because the interaction with the substrate and the particles around Refs. 25 and 26. Coupling between surface plasmons of adjacent particles produces "hot spots" with further electromagnetic enhancement. In this direction, Zhou et al.[27] reported that the detection limit of R6G can be 1×10^{-14} molL^{-1} rom well-separated silver nanorods deposited on Si substrate. Furthermore, SERS spectroscopy was used to distinguish between LSPs from an array of oblate golden spheroids and propagating surface plasmon from thin gold film, which was deposited beneath Ref. 28. Nanowires prepared by the Langmuir-Blodgett technique (LB) with length on the order of 2 to 3 microns and 50-nm diameter with pentagonal cross section exhibited a large enhancement of SERS.[29] According to the expressions of the enhancement factor of SERS due to LSP excitation, the larger gain is attainable when the excitation wavelength is close to the LSP wavelength of the particle adjacent to the probe molecule.[13] Since the enhancement comes from both the incident (exciting) field and the scattered field with shifted frequency, it is adequate to require that the LSP frequency located between the exciting and the shifted frequency. Felidj and collaborators made attempts to confirm this fact experimentally.[30]

The effect of the substrate type on the Raman scattering intensity was formally treated, for the first time, by Greenler and Slager before even the SERS phenomenon was predicted.[31] Greenler model was modified, improved, and developed recently by Liu and Zhao[32] to the case of SERS from tilted nanorods deposited on flat substrates. Although silver nanorods were and still widely used by many researchers as an attractive substrate in investigating SERS,[33–35] only few investigators examined the most optimal nanostructures for larger enhancement in terms of optimizing the size, shape, separation and substrate material.

In this work we present a study of SERS substrates based on a special type of rods in the form of thin films called sculptured thin films (STFs),[36] prepared by the glancing angle deposition technique (GLAD), which have been under investigation recently in our group for their plasmonic properties.[5,37–40] Although several works[41–44] have already been published on SERS from

Ag and Au STFs, no comparison between the different substrates materials and film deposition conditions was considered. Here, a wide manifold of silver STFs is considered and the effects of the rods length, shape, and the substrate type on SERS enhancement are considered as well as a theoretical modeling which is proposed to explain the results.

2 Samples Preparation and Experimental Setup

1. Sculptured thin films (STF), which are assemblies of shaped parallel nanowires, are prepared using many variants of the basic glancing angle deposition (GLAD) technique.[45] The growth mechanism is based on self-organized nucleation of nanoparticles and subsequent highly directional growth due to atomic shadowing of the nanoparticle flux reaching the substrate at a large oblique angle with respect to the substrate normal. With an appropriate substrate rotation during growth, the nanostructures can be varied in shape from tilted rods to helices to chevrons and recently blades.[46]

   The Ag nanorods of STFs were grown by means of electron-beam-evaporation GLAD.[47,48] The incidence angle at deposition was set to 85 deg from the substrate normal in all cases. For reference, dense films of each material were prepared with the incidence parallel to the substrate normal. Some of the films were deposited on substrates templated with monolayers of Polystyrene nanospheres using a self-assembly method and with Au dots in hexagonal arrangements gained by evaporating Au through the voids of such self-assembled films of hexagonally close-packed nanospheres with subsequent removal of the spheres as described by Fuhrmann et al.[49] After growth, the samples were examined with scanning electron microscopy (SEM) at 2.5 kV acceleration voltage. Analysis of the SEM micrographs was done using the commercially available Scanning Probe Image Processor (SPIP) (version 3.2.6.0) with the grain-detection module. A schematic illustration for the general structure of the rods is demonstrated in Fig. 1.
2. The SERS probe molecule 4-Aminothiophenol (4-ATP) was diluted in ethanol at 1 wt. %. After immersing the STFs in the solution for 24 h, the ethanol was evaporated by exposing the samples to air for about half hour. The specific vibration modes of the adsorbed molecule were considered in order to evaluate the enhancement factors of SERS from the different STFs.[50] For evaluating the detection limit, lower concentrations of 4-ATP in ethanol were used down to the order of 10^{-10} wt.%.
3. Surface enhanced Raman scattering (SERS) measurements were performed using Raman spectroscopy system (Control Development), which is equipped with a laser diode emitting at 785 nm as the excitation wavelength and having approximately

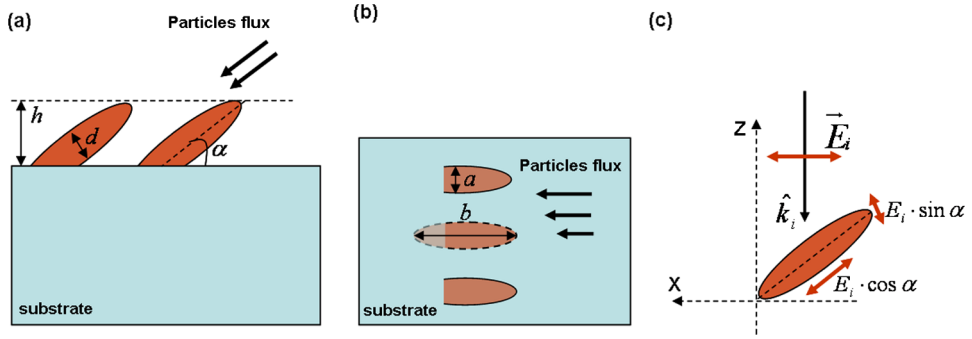

Fig. 1 Schematic illustration which demonstrates the columns creation during the evaporating process. Side view of the STF (a) Top view of the STF (b) Schematic description to the interaction between the incident electric field and the inclined columns of the STF (c). *h*- STF layer thickness, *d*- rod's diameter in the plane of the incoming vapor flux, α- rod's inclination angle measured from the substrate, *a*- rod's diameter perpendicular to the plane of the incoming vapor flux, and *b* the major axis length. E_i The incident electric field amplitude and $\hat{k}_i$ a unit vector indicates the propagation direction.

50 mW power on the samples (~80 W/cm^2). The excitation is coupled to the sample using a 200 μm core fiber and the back-scattered radiation was collected using 400 μm core fiber. For each sample, a dense film of the same material and with the same thickness deposited on similar substrate was taken as a reference. The samples were divided into subgroups in which each group has common features, and then a comparison between the different subgroups was made in order to identify the sample with the highest enhancement.

3 Experimental Results of SERS

In the first step, two types of Ag nanostructures were prepared, namely vertical columns and slanted Ag columns with varying heights. These samples were made on four different types of substrates: bare Si(100), Si(100) covered with 15-nm-thick Ti layer, fused silica (glass), and honeycomb template with 35-nm-thick Au dots. In order to pattern the substrates with growth seeds in honeycomb-like arrangement, the nanosphere lithography was used. These substrates were patterned before depositing the Ag films, to grow the nanorods in periodic arrangements. Initially, a bare silicon substrate was covered with polystyrene nanospheres of diameter $D = 517$ nm in hexagonal-close-packed arrangement. After such spreading of the nanospheres, 35-nm Au was deposited through quasi-triangular spaces (i.e., spaces through successive spheres), then the nanospheres were removed in an organic solvent and the Au dots remained in honeycomb-like arrangement [see Fig. 2(c) and 2(d)].

By varying the deposition time, the nanostructures were sculptured with different heights. The heights for both the vertical and the slanted columns were planned to be similar in the range 50 to 400 nm. This group of samples will be referred to as group A. the vertical columns are perpendicular with respect to the substrate surface, whereas slanted columns have inclination of roughly 20 to 25 deg with the substrate.

The substrate influence was examined by comparing samples with the same heights and inclination on different substrates. From Fig. 3, one can see that, nanostructures deposited on Si(100) give larger enhancement than STFs with the same features but deposited on other materials. Figure 3 shows only the results of STFs made of about 350-nm height vertical columns deposited on different substrates and compared to typical spectrum of solid 4-ATP bulk. The curves of fused silica and Si(100) with 15 nm Ti were exceptionally enlarged for

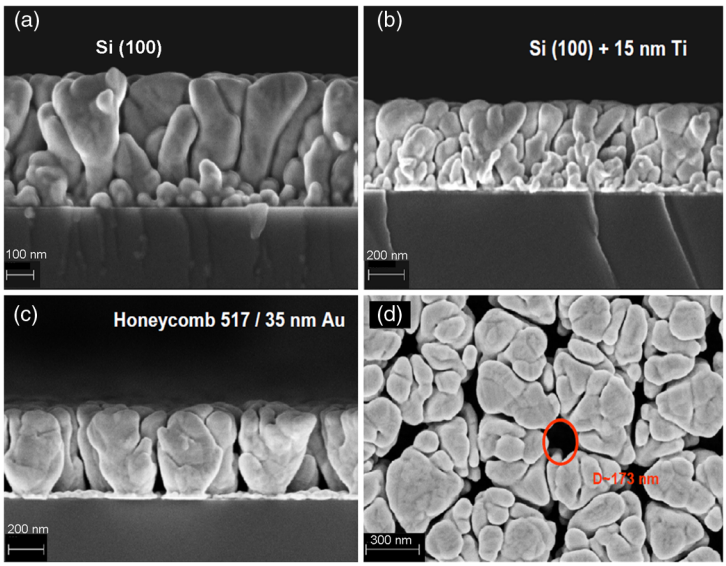

Fig. 2 Ag nanorods with ~350 nm height deposited on bare silicon substrate (a) deposited on silicon covered by 15 nm titanium thin layer (b) deposited on a prepatterned Honeycomb (517 nm diameter of sphere/35 nm Au dot) (c) top view of image c (d).

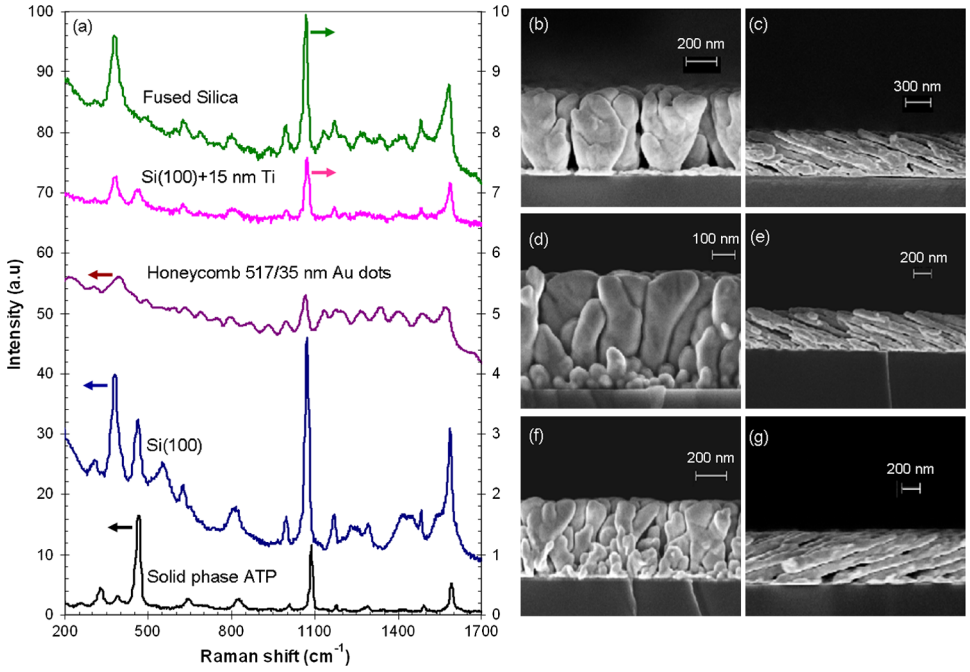

Fig. 3 Raman signals from Ag STFs with vertical columns of height nearly 350 nm that are deposited on silicon substrate (left vertical axis), silicon covered with 15 nm Ti (right vertical axis), fused silica (right vertical axis), and honeycomb 517/35 nm Au dots (left vertical axis) compared to typical spectrum from solid phase ATP (left vertical axis) (a) SEM cross section pictures of vertical columns on honeycomb 517/35 nm Au dots (b) similar to *b* with slanted columns (c) vertical columns on Si (d) similar to *d* with slanted columns (e) vertical columns on Si + 10 nm Ti(*f*) similar to *f* with slanted columns (*g*). The curves of fused silica and Si(100) with 15 nm Ti were enlarged (x10) by adding secondary vertical axis for convenience.

convenience. Although the results of the slanted columns with the same sizes are not shown here, they exhibited the same dependence with the substrate material. This behavior of the STFs versus the substrate type was repeatable and independent of the columns height for almost all the size categories in this group of samples.

The interference fringes of the signal obtained from the honeycomb template substrates are most likely due to the periodic order of the nanostructures composing these substrates as can be seen from Fig. 3(b). Since the columns that were deposited on the bare silicon substrates gave the largest enhancement with respect to the other substrates, the examination of other features within this group of samples was focused on these types of STFs, namely Ag columns on silicon substrates.

The actual heights of the nanostructures that were grown on silicon in this group were in the range of 50 to 350 nm for the vertical columns and in the range 50 to 400 nm for the slanted columns. Although the height effect was examined for all the substrates, Fig. 4 presents only the Raman intensity obtained from those that were deposited on silicon. The actual heights of the columns as they were estimated from the SEM images are slightly different from the planned heights of the nanostructures. Figure 4(a) shows Raman scattering intensity obtained by the vertical columns V1-V4 with heights as estimated from the SEM images are 50, 150, 250, and 400 nm, respectively. Figure 4(b) shows the SERS from the slanted columns S1 to S4 with their estimated heights being 50, 120, 250, and 400 nm, respectively. The scattering from closed thick Ag film on Si was recorded and compared with the results of both the vertical and slanted columns. The Raman signal obtained from closed film response is considerably below the noise level, which clearly emphasizes the prominent contribution of the nanostructures to SERS enhancement. Both the measurement results from the vertical and the slanted columns show that there is an optimal height of the columns in which the enhancement factor of SERS is the largest when the size-based comparison is considered. Furthermore, one can see from Fig. 4

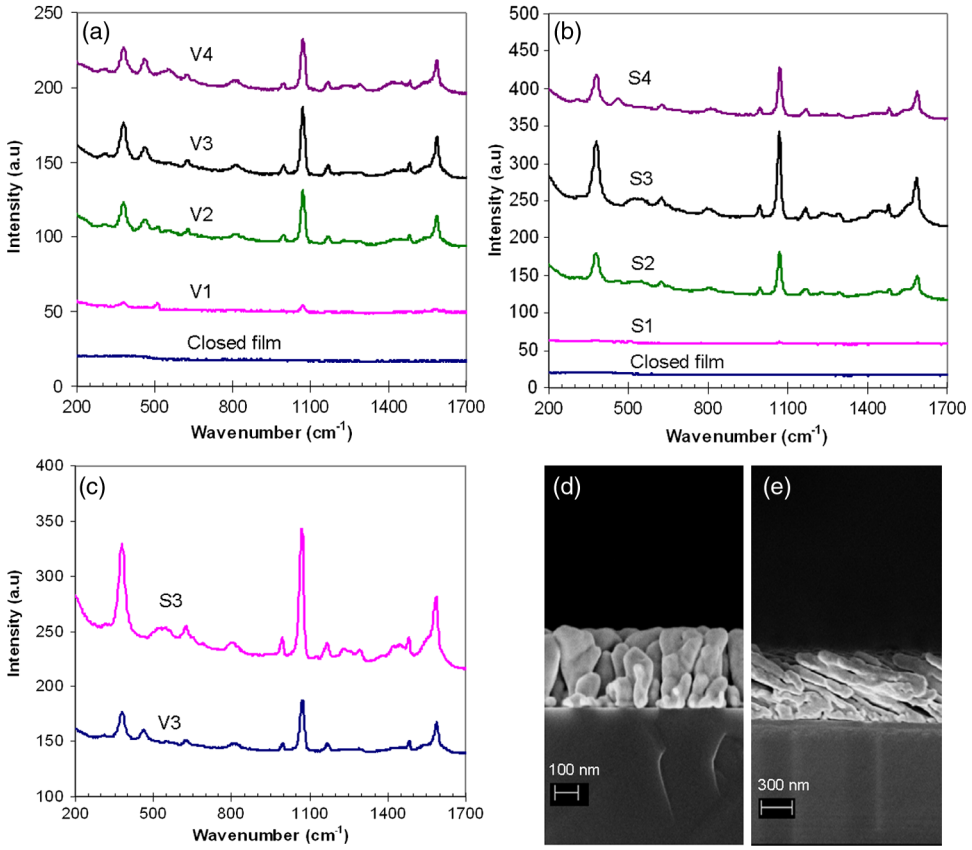

Fig. 4 Raman intensity of the vertical columns in group A with different heights V1–V4 deposited on Si(100) (a) Slanted columns with different heights S1–S4 on Si(100) (b) Comparison between S3 and V3 enhancement (c) Side view SEM image of V3 (d) SEM cross section image of S3 (e) The scattering from 300 nm thick closed Ag film on Si(100) is presented for comparison in both (a) and (b) The heights of the vertical and slanted columns are mentioned in the text.

that this optimal height located in the range 300 to 400 nm in both cases of vertical and slanted columns with a slight advantage to the sample with the slanted columns.

Since the size and shape of the nanostructures that composed the STFs is a key feature in determining the SERS enhancement, another group of samples was prepared to examine this effect extensively. Group B consists of only vertical columns with six different heights. The measured heights and widths of the rods are given in Table 1 as well as the originally planned height values. Each sample of group B was deposited on two different substrates, bare Si(100) and bare Si(100) with 45-nm Ag layer above. The purpose of adding the flat 45-nm Ag film

Table 1 The planned and actual heights of some of the films in group B. The deposition time and columns diameter are also given.

Sample no.	Planned height (nm)	Deposition time (min)	Column width (nm)	Column approx. number density (μm^{-2})	Measured film height (nm)
1	50	31	76 ± 34	65 ± 11	58
2	100	62	140 ± 47	43 ± 11	97
3	200	124	171 ± 42	22 ± 9	192
4	300	187	188 ± 53	20 ± 6	289
5	500	250	204 ± 41	18 ± 3	442
6	600	300	231 ± 39	11 ± 2	487

underneath the STF is to test the conclusions of some previous studies on SERS, which reported the advantage of adding this film.[32]

The effect of the shape of a nanorod on the LSPR is often characterized by the aspect ratio. The nanostructures in group B approximately have a spheroid shape with the diameter in the plane of the incoming vapor flux and the diameter perpendicular to this plane are approximately equal. In this case the aspect ratio of the rods is defined as the ratio between the long major axis perpendicular to the substrate and the short axis parallel to the substrate (see Fig. 1). One of the major requirements from the new samples group is to examine the aspect ratio effect on the enhancement factor. Basically, in order to perform this examination, the heights of the films are required to vary while the rods diameters are kept fixed.

Although Fig. 5(a) demonstrates that STF with 442-nm rod's height has the largest SERS enhancement factor, several clarifications of the deposition process should be taken into consideration. In fact, the deposition rate for all the films was kept constant; however, the films thicknesses are different from the planned values (see Table 1). This could be a result of some early mounds that are formed at the substrate surface, which become broader as the film thickness increases. Consequently, column number density (i.e., column number per unit area) decreases with respect to increasing film thicknesses due to competitive growth mode under shadowing condition. Additionally, as one can see from the SEM micrographs for the layers with 58 and 97 nm heights [see Fig. 5(c)], the columns are interconnected with each other. Similarly, for the thicker layers there might be identical bases, which are interconnected with neighbors but from the top view SEM micrographs the columns are separated [Fig. 5(d)]. However the overall columns growth process is strongly influenced by the nucleation layer (i.e., early growth islands). One can conclude from the SEM images that when the STF height is small, the nanostructures are formed in islands-like shapes and don't have the columnar shape as STFs with larger height. Because of these limitations in the deposition process and the scaling between the deposition time and the columns widths, the obtained aspect ratios of the films in group B were not precisely as planned. For the same reasons the layers that were deposited on 45 nm Ag thin film have columns that are very close to each other or even merged

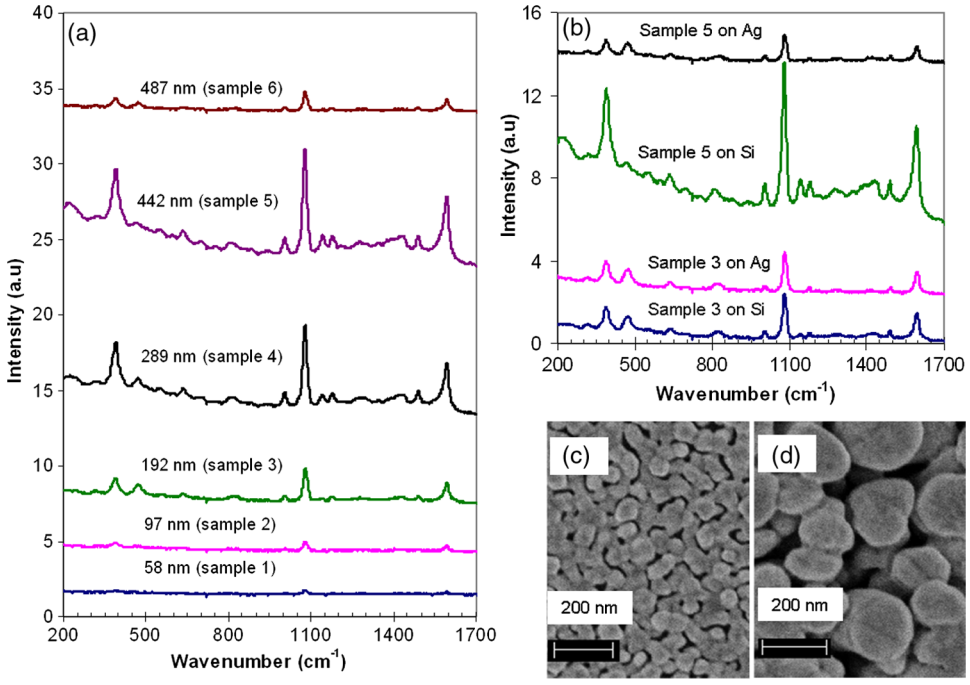

Fig. 5 Raman intensity of Ag STFs with different heights deposited on bare Si substrate (a) Comparison between the Raman signal of STF deposited on bare Si substrate (sample 3) and STF on 45 nm Ag film (sample 5) (b) Top view SEM image of sample 1 (c) Top view SEM image of sample 5 (d).

together. The actual dimensions of the layers as they were estimated after the deposition process are given in Table 1.

Figure 5(b) demonstrates the comparison between STFs that were deposited on bare Si substrate and those that were deposited on Si with additional 45-nm closed film above. Although the comparison is shown for two heights, one can see that there is no advantage to the Ag thin film beneath the columns; on the contrary, this additional layer may decrease the enhancement for larger columns.

To deduce the enhancement effect of SERS from 4-ATP on these substrates quantitatively, the enhancement factor (EF) values of a monolayer of 4-ATP on STFs were calculated according to acceptable procedure in the literature.[51,52] The EF was calculated according to the following expression:

$$\mathrm{EF} = \frac{I_{\mathrm{SERS}}}{I_{\mathrm{bulk}}} \cdot \frac{M_{\mathrm{bulk}}}{M_{\mathrm{ads}}}, \tag{1}$$

where I_{SERS} is the SERS intensity of a specific vibrational mode from 4-ATP on STF, and I_{bulk} is the intensity of the same vibrational mode from the solid phase of the sample. When the solid phase spectrum is considered, M_{bulk} the number of molecules that are exposed to the laser beam is calculated from $M_{\mathrm{bulk}} = A_{\mathrm{laser}} \cdot d_{\mathrm{pen}} \cdot N_m$. The multiplication of the spot size A_{laser} and the penetration depth of the beam inside the solid sample d_{pen} gives the volume of the laser beam portion inside the sample, and N_m is 4-ATP molecules number density in the solid state.

For the SERS spectrum, the number of the adsorbed molecules M_{ads} at the STF surface can be calculated by: $M_{\mathrm{ads}} = C \cdot \{A_{\mathrm{laser}} \cdot P_{\mathrm{den}}\} \cdot \{S_p/S_m\}$. Here P_{den} is the columns density of the STF (columns per unit area), S_p is the single column entire surface area, and S_m is the area occupied by single 4-ATP molecule when it is adsorbed to the STF. The coefficient C expresses the 4-ATP concentration in 4-ATP/Ethanol solution in which the STF was dipped. This correction factor is essential in particular when the molecules number in the solution is below the full coverage limit. Considering the Ethanol density 0.789 gr/lit, 4-ATP molecular weight 125.19 gr/mole, and 4-ATP weight concentration 0.01, the 4-ATP molecules number in 0.25 ml the volume in which the STFs were dipped, is about 9.5×10^{18} molecules. On the other hand, the numbers of 4-ATP molecules that are needed to ensure full coverage at the surfaces of the samples 1 to 6 are 1.39×10^{14}, 2.37×10^{14}, 2.54×10^{14}, 4.27×10^{14}, 6.37×10^{14}, and 4.86×10^{14}, respectively. These numbers were calculated using the entire surface of the columns, the area occupied by single 4-ATP molecule (0.2 nm^2), and the STF area, which is about 25 mm^2. One can see that 1% 4-ATP weight concentration in the solution is absolutely sufficient to ensure full coverage of 4-ATP monolayer at each of the samples presented. Hence we set C to unity in our calculations of the EFs.

In order to apply the EF calculation procedure, the Raman scattering from the solid phase 4-ATP was acquired under the same experimental conditions as the STF layers and plotted together with the SERS spectrum of sample 4 in Fig. 6. Considering depth of field of about 1 mm of the laser beam, and spot diameter at the sample of 0.2 mm, the enhancement factors of the prominent 4-ATP peaks were calculated and given in Table 2.

The area occupied by a single 4-ATP molecule is about 0.2 nm^2 (Ref. 53), which is the theoretical lower limit of the molecule footprint. Since the 4-ATP molecule is perpendicular to the surface,[32] only the field's component normal to the surface contributes to the SERS spectra. Moreover, due to the lightening rods effect, the molecules located near the upper edges of the columns are expected to be more significant to enhancing SERS. Therefore, the calculated EFs when the entire surface area of the columns is considered will likely be an underestimate rather than an overestimate. Nevertheless, EFs on the order of 10^7 is a remarkable result compared to other structures that were recently presented by other groups such as rings, dimmer nanocubes, Ag nanowires, and high aspect ratio Ag nanorods with EFs of 4.2×10^6, 3×10^6, 2×10^5, and 2×10^6, respectively.[16,29,54,55]

Three strong bands at 1593, 1079, and 394 cm^{-1} can be observed for the 4-ATP molecules on the Ag STF [Fig. 6(b)], which are the A_1 modes of the 4-ATP molecule.[56] In addition, a weak band at 1147 cm^{-1}, which is the B_2 modes of 4-ATP molecule, was observed. Although some of the vibrational bands of 4-ATP could be enhanced due to the metal-to-molecule charge-transfer

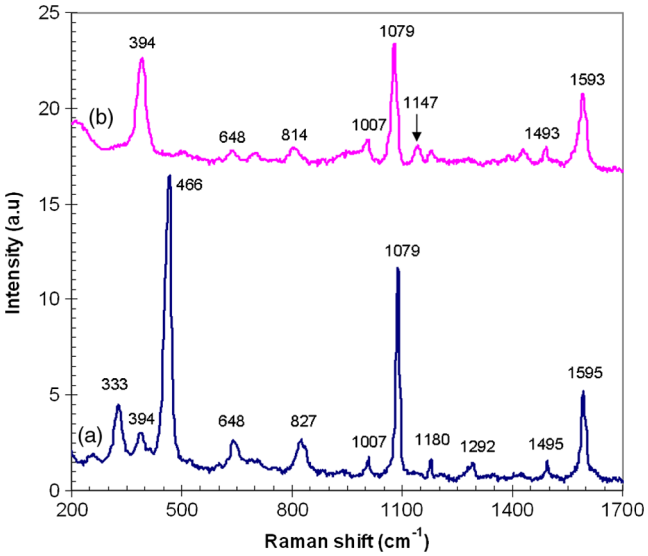

Fig. 6 (a) Raman intensity of solid phase ATP with the most prominent vibrational modes of the probe molecule, (b) SERS spectrum measured from sample 4 of group B after it was dipped in ATP\Ethanol solution with 1% wt. ATP concentration. The integration time of the two spectra was 20 seconds.

Table 2 Calculated EF values for 4-ATP on the different samples of group B for different vibrational modes. Samples 1 to 6 are the same samples that are indicated in Table 1.

	394 cm^{-1}	648 cm^{-1}	827 cm^{-1}	1007 cm^{-1}	1079 cm^{-1}	1180 cm^{-1}	1495 cm^{-1}	1595 cm^{-1}
Sample 1	0.8×10^{6}	0.6×10^{5}	0.5×10^{5}	0.2×10^{6}	0.7×10^{5}	0.2×10^{6}	0.1×10^{6}	0.1×10^{6}
Sample 2	0.1×10^{6}	0.7×10^{5}	0.6×10^{5}	0.2×10^{6}	0.7×10^{5}	0.2×10^{6}	0.9×10^{5}	0.1×10^{6}
Sample 3	0.3×10^{7}	0.16×10^{6}	0.15×10^{6}	0.5×10^{6}	0.2×10^{6}	0.4×10^{6}	0.2×10^{6}	0.4×10^{6}
Sample 4	0.5×10^{7}	0.17×10^{6}	0.12×10^{6}	0.7×10^{6}	0.4×10^{6}	0.5×10^{6}	0.3×10^{6}	0.5×10^{6}
Sample 5	0.3×10^{7}	0.9×10^{5}	0.8×10^{5}	0.4×10^{6}	0.2×10^{6}	0.3×10^{6}	0.2×10^{6}	0.3×10^{6}
Sample 6	0.7×10^{6}	0.4×10^{5}	0.3×10^{5}	0.1×10^{6}	0.6×10^{5}	0.1×10^{6}	0.6×10^{5}	0.8×10^{5}

mechanism, which largely depends on the energy of excitation and the metal surface potential, the STF substrate causes a large increase in the intensity of the overall spectra. The significant contribution of the EM to the enhancement can be easily explained by the very weak signals that were obtained from the closed films [Fig. 4(a) and 4(b)].

Vibrational frequencies and relative Raman scattering cross sections of SERS spectra are generally different from those measured in fresh samples due to the CM effect. As a consequence, additional bands may become observable in SERS spectra, or existing bands may be attenuated beyond the detection limit.[57,58] While the EM effect can extend up to a few tens of nanometers, the CM effect is extremely localized in nature. When sample molecules come close to the metal atoms, typically at molecular distances, the sample molecules may get adsorbed on the metal and make chemical bonds with metal atoms. This usually happens with a transfer of charge from the metal to the sample molecule. The chemical bonds on one hand restrict the natural vibration of free molecules resulting in modified vibrational frequencies of adsorbed molecules; on the other hand, the charge transfer results in resonance effect, enhancing the overall Raman scattering from the adsorbed molecules. In fact, the charge transfer serves as the intermediate stage of the resonance Raman process in the CM effect. Thus the CM effect adds up in enhancement and results in shift of the vibrational frequencies.[59]

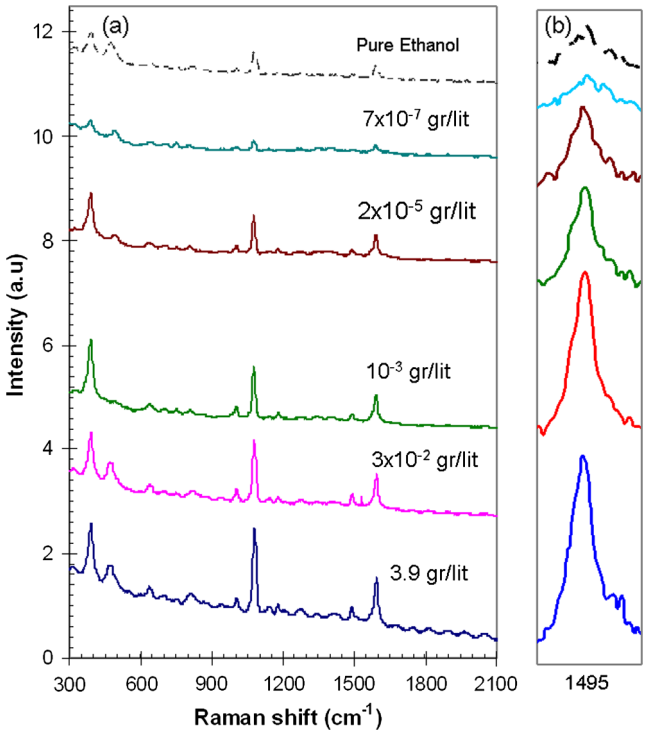

Fig. 7 SERS from STF with 500 nm height deposited on thin 50 nm Ag film on Si substrate for different ATP in Ethanol concentrations. The corresponding ATP concentrations for the curves are given near each curve in ATP grams per Ethanol liters (a) The peak located at 1495 cm^{-1} intensity versus ATP concentrations that were addressed in part a of the figure.

Since SERS is often used for biomolecules detection, the low detection limit of ATP from STF was also examined. For this purpose, 4-ATP was diluted in ethanol with different concentrations. One can notice from Fig. 7 that remnants of some of the vibrational modes are observable even when the STF is dipped into pure ethanol. These are perhaps due to C-C or C-H related chemical bonds that evolve from the surface ethanol interaction. In fact, the observation of these Raman peaks is clear indication that single molecules are indeed observed on the surface. On the other hand, no bands of the pure bulk ethanol are observed from the STFs SERS spectra since the samples were thoroughly dried from the ethanol before acquiring the SERS spectra. In order to make our sensing examination more realistic and unique, we used the peak at 1495 cm^{-1}, which obviously appears in the solid phase 4-ATP spectrum and in the 4-ATP on the STF spectrum as well, while it approximately disappears in the spectrum obtained from the pure ethanol.

The 4-ATP concentration in ethanol varies from 0.5% wt (4 gr/lit) down to 9.6×10^{-10}% Wt (7×10^{-7} gr/lit) until the intensity of the peak at 1495 cm^{-1} vanishes. One can see from Fig. 7(a) that a concentration of 0.7 μg/lit of 4-ATP can be easily detected by some of the STFs substrates. It should be also noted that the STF that was used in Fig. 7 is not the optimal structure that we found before. Hence the actual smaller detection limit is expected to be smaller than this value.

4 Discussion

The Raman intensity from the STFs was initially compared to the reference samples, which are the counterpart-closed films. In the case of flat surface, there are several models that can describe the electromagnetic interactions between the adsorbed molecule and a flat metal surface.[12] The enhancement occurs due to the fact that the molecule near the surface is illuminated by both a direct and a reflected field, which are coherently superimposed to give intensity up to

four times the incident intensity. Likewise, the Raman scattered field is composed of a direct and reflected field yielding up to fourfold an increase in its intensity leading to up to total maximum enhancement by factor of 16.

Treating roughness features, on the other hand, was done by considering a small metal ellipsoid, near which the adsorbed molecules are placed. The dipole moment induced in an adsorbed molecule will be due both to the incident field and the field elastically scattered by the metal ellipsoid. For ellipsoids small compared to the wavelength of light, this scattered field becomes much larger than the incident field when the frequency becomes resonant with the dipolar surface plasmon. This may be regarded as a field concentration effect in a limited region of space in the vicinity of the ellipsoid. Moreover, the Raman-scattered field will, for small Raman shifts, become resonant or near resonant with the surface plasmon of the metallic particle causing the field scattered by the metal particle to be unusually large. That is, the scattered power received from the oscillating molecule will be unusually large as a result of this resonance. Recently, the quantitative nature of the electromagnetic enhancement effect on SERS was studied by Yoshida et al.[60] The validity of this effect both theoretically and experimentally was absolutely demonstrated using metallic isolated nanostructures.[61]

In order to basically examine the experimental results, our STF layers are modeled as arrays of identical and parallel spheroids on which the probe molecules are adsorbed. The model that is described in the appendix basically gives an insight into the enhancement process caused due to the LSPR excitation of the nanostructures that composed the STF. The spheroid EM model presented here still does not describe the realistic experimental results exactly because it treats each nanorod as independent from the others. Since the model considers the enhancement for an isolated particle, the effects of the substrate and coupling between adjacent particles on the enhancement magnitude and shape, which are important, were not considered in this model. Since the results that are presented here are obtained within a comparative study, the spheroid EM model can provide basic qualitative explanation to the major results.

More exact numerical calculations were presented by Yang et al.[62] using the discrete dipole approximation (DDA) method to determine extinction and Raman intensities for small metal particles of arbitrary shapes. The coupling between adjacent particles and the influence of the substrate were examined, although in their calculations only two particles were considered, it still gives a representative description in the case of particles array. A comparison between the spheroid EM model and the DDA method results did not exhibit significant differences between the enhancement shapes. A little red-shift in the resonance wavelength and suppression of about 15% in the intensity were observed in the case of two coupled particles compared to the enhancement obtained from single identical particle in the DDA method. Similar behavior of the resonance wavelength was also observed when the spheroid particle was approached to a flat substrate, with an extremely small increase in the enhancement magnitude. Another comparison of the spheroid EM model was done with exact electrodynamics calculations using the T-matrix method.[63] Reasonable agreement was obtained between the results of the spheroid EM model approximation and the T-matrix method results, except slight differences in the resonance wavelengths that may be also affected by the differences in the metal particle dispersion that was considered in the two methods. Since we present here a comparative study, the enhancement results that are estimated from the spheroid EM model could be accounted as a reasonable tool in analyzing the experimental results. Also, as one can see easily from the SEM micrographs, the rods size and width have some distribution, which also needs to be taken into account in an exact model.

In the earlier stages of our study, different materials were examined from the aspect of enhancing Raman intensity. Since silver exhibited the largest enhancement among these materials, it was solely used in presenting the current evidences. Considering Eq. (A2) in the appendix, close to the resonance region which is defined by $\varepsilon_{\mathrm{ir}} = -\chi_i \cdot \varepsilon_0$ where $\varepsilon_{\mathrm{ir}}$ is the real part of the dielectric constant of the nanostructures, one can see that the enhancement is proportional to the factor: $|g(\lambda_{\mathrm{ex}})|^2$. If we compare between different materials with the same particles shape, we find that $|g(\lambda_{\mathrm{ex}})|^2$ is in particular governed by the ratio $(\varepsilon_{\mathrm{ir}}/\varepsilon_{\mathrm{ii}})^2$. The ratio between the real and the imaginary parts for silver at the excitation wavelength is the highest among the other materials that were examined.

Another direct consequence of the EM model shows that increasing the aspect ratio of the spheroid causes a red-shift in the resonance wavelength and broadening in the enhancement shape. The red-shift is caused by increasing the rotational axis length; in particular when the polarization state of the incidence field is parallel to this axis, and the resonance wavelength is proportional to this length. The increase in the maximum enhancement, on the other hand, is due to the lightning-rod effect in which the enhancement is maximized at the tips of the spheroid [see Fig. 8(a)]. When the total size of the particle increases while keeping the aspect ratio fixed, the resonance wavelength will be red-shifted, and the enhancement profile becomes wider with a significant suppression to the maximum enhancement [Fig. 8(b)]. This in fact shows the electrodynamics correction effect, which is more significant when the particles are larger. The trade-off between these two effects can simply explain the fact that there is an optimal height in which the enhancement is largest.

Considering the latter consequences of the enhancement profile, one can state that the shape and size basically govern the polarizability of the nanostructures and hence affect the LSPR wavelength and the enhancement shape. The substrate type, on the other hand, modifies the effective refractive index (RI) of the hosting medium of the nanostructures, which affects the LSPR wavelength location as well.[64] So the combination of the height of the optimal structure that was presented in Fig. 4 together with the substrate where the nanostructures are deposited is probably responsible to the final location and shape of the enhancement profile. The entire effect of the size, shape, and substrate type increases the overlap between the enhancement profile and the exciting laser band, which, by the end, is realized by the large SERS enhancement from this optimal STF. This interpretation can hold for both the optimal structures from group A and B that were presented in Figs. 4 and 5, respectively.

When the elongated rods are inclined with respect to the surface, both the lateral and the longitudinal modes of the LSPR can be excited, which is expected to positively contribute to the total enhancement [see Fig. 1(c)]. The additional contribution to the enhancement due to exciting the longitudinal LSPR may be more significant when the nanostructure is more elongated and that is caused due to the large enhancement caused by the major axis mode compared to that of the equatorial axis. The superposition of the two LSPR modes can interpret the advantage of the slanted columns, which was demonstrated in Fig. 4(c).

The islands involved in the beginning of the deposition process constitute the bases of the rods and therefore have a significant effect on the final shape of the nanostructures and their

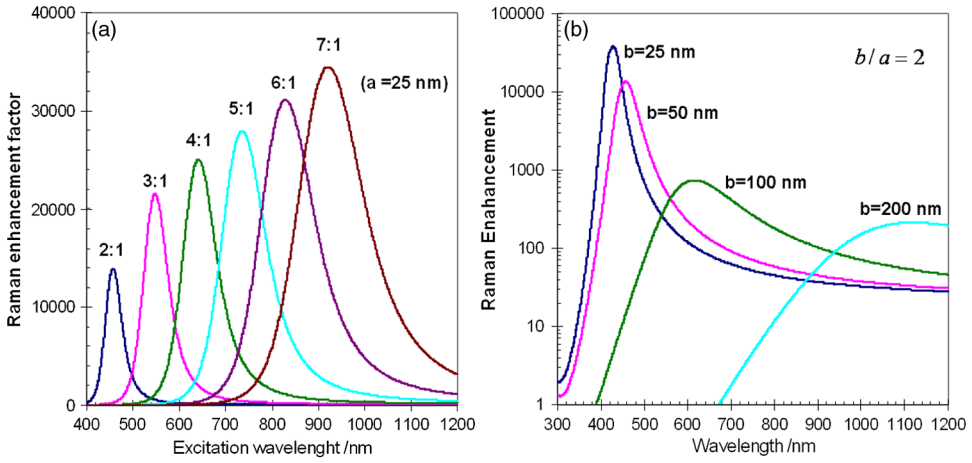

Fig. 8 Raman enhancement factor calculated using equations A1 and A2 in the appendix when the electrodynamics correction is considered and the Raman frequency shift is 1010 cm^{-1}. The curves correspond to silver prolate spheroid with fixed equatorial semi-axis equals 25 nm and various aspect ratios. The incident field is polarized parallel to the rotational axis and the surrounding medium is air with dielectric constant equals unity (a) Raman enhancement factor for silver prolate spheroid with fixed aspect ratio equals 2 embedded in air. The rotational semi-axis is varied from 25 nm to 200 nm and the polarization of the incident field is parallel to the major axis (b).

separation. This apparently was the reason for obtaining smaller enhancement from STFs that were deposited onto Si with thin silver film. This effect disturbs the final shape of the nanostructures and becomes stronger when the rods of the STF are larger [see Fig. 5(b)]. The disturbance in the uniform shape of the nanostructures due to these connected bases expands the distribution of the structures sizes, which broadens and spreads the LSPR spectra. Samples that were deposited on Si substrate, on the other hand, were more separated and uniform; hence their enhancement profile is expected to be more defined and sharper. Furthermore, we believe that this mounds effect is also responsible for the differences between the enhancement obtained from Si and Si with Ti substrates. Since the differences between the compositions of these substrates are not expected to be so significant, the larger enhancement obtained from STFs on Si is due to the more separated columns with respect to those that were created on the Si and Ti substrates [see Fig. 3(d) and 3(f)].

A note should be finally added on STFs with small thickness as they can in fact be considered as islands, which were extensively reported as attractive substrates for SERS and SEF.[65,66] However the nanostructures are still interconnected, this islands-like shape can obviously be observed from Fig. 5(c). Comparison of STFs with larger heights and in particular those with the optimal height with these islands-like shapes shows that the STFs with the columnar shape still have clear supremacy upon the islands-like structures, which in turn could be counted as being a more credible comparison when evaluating SERS enhancement with respect to other substrates. In addition, for different excitation wavelengths, one needs different rod heights and different aspect ratios, which cannot be controlled efficiently with metal islands.

At last, one more comment should be added on the long-term stability of the STF structure. Some of the samples were kept in standard lab conditions without any particular protection procedures. The SERS enhancement factors from these samples after one year were not significantly harmed due to the aging effect. We believe that the stability of these films can be considered as a very remarkable feature, which should be further investigated in the future.

5 Conclusions

Comparative detailed study of surface enhanced Raman scattering (SERS) from silver nanosculptured thin films (STFs) was presented. The STFs were deposited on different substrates with various shapes and sizes. The STFs used are assemblies of tilted, shaped, parallel nanostructures prepared with several variants of the oblique angle deposition (GLAD) technique. The influence of the topologies and the substrate features on the enhancement of SERS were studied. Comparison between the different films indicates that the enhancement factor is higher when the nanostructures made from silver and deposited onto silicon substrate. Enhancement factors on the order of 10^7 were obtained from silver nanorods deposited on bare silicon substrate with respect to their dense film counterparts using 4-Aminotheophenol for the Raman emission. The low detection limit that can be achieved with STFs is below 1 μg/lit of the probe molecule 4-ATP in ethanol solution. Adding a thin silver film underneath the Ag nanorods did not increase the enhancement factor compared to those obtained with bare silicon bulk. The STFs exhibited extraordinary stability despite the fact that silver is reactive and not stable against environmental conditions.

Theoretical model based on the spheroid EM mechanism was used to explain qualitatively the experimental results. Modeling the layers as arrays of separated and isolated spheroid-like particles qualitatively interprets the relative enhancement factors that were obtained by the experiments. When the dimensions and the aspect ratio of the particles produce localized plasmon with its resonance wavelength coinciding with the laser excitation wavelength, maximum Raman enhancement factors could be obtained. Due to their high enhancement and reproducibility, silver STFs could serve as prominent substrates for biosensing.

Appendix

Assuming that the adsorbed molecules are randomly distributed on the surface of a prolate spheroid much smaller than the excitation wavelength and which its major semi-axis is -b and its

equatorial semi-axis is -a (see Fig. 1), the total averaged Raman enhancement EN following Schatz[67] is:

$$\mathrm{EN} = \Re(\lambda_{ex}) \cdot \Re(\lambda_{sc}). \tag{A1}$$

The components $\Re(\lambda_{\mathrm{ex}})$ and $\Re(\lambda_{\mathrm{sc}})$ refer to the enhancements in the incident and the scattered fields, respectively. When doing this, we also make the simplifying approximation that the field enhancement for the Raman-emitted photon with wavelength λ_{sc} can be calculated by using the same expression for the field as the incidence photon with the excitation wavelength λ_{ex}. The SERS enhancement factor is then proportional to $|E(\lambda_{\mathrm{ex}})|^2 \cdot |E(\lambda_{\mathrm{sc}})|^2$ which was indicated by $\Re(\lambda_{\mathrm{ex}})$ and $\Re(\lambda_{\mathrm{sc}})$ in Eq. (A1). If the spheroid is small compared to the wavelength of light, the local field $E(\lambda)$ can be obtained by solving Laplace's equation when the surrounding medium is replaced by an effective dielectric constant. Under the former assumptions, the field intensity enhancement at the surface is given by:

$$\Re(\lambda_{\mathrm{ex}}) = |1 - g(\lambda_{\mathrm{ex}})|^2 + \left[\frac{2 \cdot \mathrm{Re}\{[1 - g(\lambda_{\mathrm{ex}})] \cdot g^*(\lambda_{\mathrm{ex}})\}}{Q_1(\xi_0)} + \frac{|g(\lambda_{\mathrm{ex}})|^2}{Q_1^2(\xi_0) \cdot (\xi_0^2 - 1)}\right] \times \left[\frac{-(\xi_0^2 - 1)^{1/2} + \xi_0^2 \cdot \sin^{-1}(1/\xi_0)}{(\xi_0^2 - 1)^{1/2} + \xi_0^2 \cdot \sin^{-1}(1/\xi_0)}\right], \tag{A2}$$

where the parameter $\xi_0^2 = (1 - a^2/b^2)^{-1}$ represents the aspect ratio of the spheroid-(a/b), and $Q_1(\xi_0)$ is the Legendre function of the second kind which is given by:

$$Q_1(\xi_0) = \frac{1}{2}\xi_0 \ln\left(\frac{\xi_0 + 1}{\xi_0 - 1}\right) - 1, \tag{A3}$$

and $g(\lambda_{\mathrm{ex}})$ is a gain parameter, which depends on the dielectric constants of the spheroid and the medium evaluated at the excitation wavelength.

$$g(\lambda_{\mathrm{ex}}) = \frac{\varepsilon_i - \varepsilon_0}{\varepsilon_i + \chi_i \cdot \varepsilon_0}. \tag{A4}$$

Here $\varepsilon_i = \varepsilon_{\mathrm{ir}} + i \cdot \varepsilon_{\mathrm{ii}}$ and ε_0 are the dielectric constants of the spheroid and the surrounding medium respectively at the excitation wavelength, and the shape dependent parameter $\chi_i = (1/D_i) - 1$. The depolarization factor D_i is determined according to the incident field polarization state. If the incidence field is polarized parallel to the major axis of the spheroid, the parallel depolarization factor D_i is given by:[68]

$$D_i = D_{\mathrm{par}} = \frac{1}{(a/b)^2 - 1} \cdot \left[\frac{(a/b)}{[(a/b)^2 - 1]^{1/2}} \cdot \ln\{(a/b) + [(a/b)^2 - 1]^{1/2}\} - 1\right]. \tag{A5}$$

If the incidence field is polarized parallel to the equatorial axis of the spheroid, the perpendicular depolarization factor will be: $D_{\mathrm{Per}} = (1 - D_{\mathrm{Par}})/2$

$$D_{\mathrm{per}} = \frac{1}{2 \cdot ((a/b)^2 - 1)} \cdot \left[(a/b)^2 - \frac{(a/b)}{[(^a/b)2 - 1]^{1/2}} \cdot \ln\{(a/b) + [(a/b)^2 - 1]^{1/2}\}\right]. \tag{A6}$$

The component $\Re(\lambda_{\mathrm{sc}})$ is calculated in the same manner as $\Re(\lambda_{\mathrm{ex}})$ when the excitation wavelength is replaced by the Stokes wavelength λ_{sc}. The enhancement factor for a sphere with a radius (a) that is much smaller than the wavelength $(a \ll \lambda_{\mathrm{ex}})$ was early developed by Kerker et al.[10] as follows:

$$\mathrm{EN} = |[1 + 2 \cdot g(\lambda_{\mathrm{ex}})] \cdot [1 + 2 \cdot g(\lambda_{\mathrm{sc}})]|^2. \tag{A7}$$

The gain parameter of the sphere $g(\lambda_{\mathrm{ex}})$ is determined as in Eq. (A4) when the shape dependent parameter $\chi_i = 2$, ($D_i = 1/3$ for sphere). The enhancement appears in Eq. (A7) is size independent due to the first-order approximation of $g(\lambda_{\mathrm{ex}})$ and $g(\lambda_{\mathrm{sc}})$ used in the analysis. To extend this analysis to include small spheres with $2\pi a/\lambda_{\mathrm{ex}}$ as large as 0.1, a higher-order

approximation for the gain factors should be incorporated, and accordingly the factors $g(\lambda_{ex})$ and $g(\lambda_{sc})$ are redefined as follows:

$$g(\lambda_{ex}) = \frac{\left[(\varepsilon_i - \varepsilon_0) - \frac{(k_0 a)^2}{10}(\varepsilon_i^2 - 1)\right]}{\left[(\varepsilon_i + 2 \cdot \varepsilon_0) - \frac{(k_0 a)^2}{10}(10 - 9\varepsilon_i - \varepsilon_i^2)\right]}. \tag{A8}$$

The last expression is also valid when the spheroid and the medium dielectric constants are evaluated at the scattered wavelength λ_{sc}, and the wave number k_0 is replaced by the wave number at the scattered wavelength. The expression given in Eq. (A2) for spheroidal particle is also size independent and determined only by the aspect ratio of the particle. This is a result of the electrostatic limit approximation that holds for small particles. When the spheroid dimensions become larger, the radiation of the induced dipole reduces the polarization induced by the applied field, an effect known as the radiation damping effect.[69] Moreover, the interference between the radiations emitted at different points on the surface of the particle should be taken into account for larger particles. The second effect is known as the dynamic depolarization effect. These two effects lead to dynamic correction to the Maxwell's equations solution in the static limit and can be expressed by means of a "modified induced dipole" as follows:

$$\mu_{ind} = \left(\frac{1}{1 - \frac{\alpha_o k^2}{b} - \frac{2ik^3\alpha_o}{3}}\right)\alpha_o \cdot E, \tag{A9}$$

where E is the applied field, α_o the spheroid polarizability in the static limit, and the expression in the parentheses is the electrodynamics correction factor. To incorporate this correction into the Raman enhancement factor $\Re(\lambda)$, we multiply $\Re(\lambda)$ in Eq. (A2) by the absolute square of the term in the parentheses.[14]

In addition to the electrodynamics corrections for large particles, there is a size dependent correction required when the particle is very small. It is known that the dielectric constant of a metal particle becomes size dependent whenever the particle is smaller than the conduction electron mean-free path.[70] For noble and alkali metals, this applies to particles that are roughly smaller than 20 nm in its smaller dimensions.[71] In this work the dependence of the dielectric constant of the metal spheroid on its size is not considered because the layers dimensions in our case are larger than this limit. However, the main effect of the increase in plasmon width associated with decreased particle size is the suppression of the field enhancement without changing its resonance wavelength or its shape dependence.

Acknowledgments

This research is supported by the Singapore National Research Foundation under CREATE programme: Nanomaterials for Energy and Water Management and by the Graduate school 'BuildMoNa (University Leipzig, Germany) funded within the German Excellence Initiative of the Deutsche Forschungsgemeinschaft (DFG). We would like to thank Prof. Akhlesh Lakhtakia and Dr. Christian Patzig for their support in the initial stages of this project. C.K. and J.B. fabricated the STF samples and performed the SEM images under the guidance of B.R. A.S. performed the design of the samples, the SERS measurements and analysis under the supervision of I.A. I.A. was responsible for the overall research and manuscript preparation.

References

1. M. Fleischmann, P. J. Hendra, and A. J. McQullan, "Raman spectra of pyridine adsorbed at a silver electrode," *Chem. Phys. Lett.* **26**(2), 163–166 (1974), http://dx.doi.org/10.1016/0009-2614(74)85388-1.
2. A. Campion and P. Kambhampati, "Surface-enhanced Raman scattering" *Chem. Soc. Rev.* **27**(4), 241–250 (1998), http://dx.doi.org/10.1039/a827241z.

3. P. B. Catrysse and S. Fan, "Propagating plasmonic mode in nanoscale apertures and its implications for extraordinary transmission," *J. Nanophoton.* **2**, 021790 (2008), http://dx.doi.org/10.1117/1.2890424.
4. R. Luchowski et al., "Plasmonic platforms of self assembled silver nanostructures in application to fluorescence," *J. Nanophoton.* **4**, 043516 (2010), http://dx.doi.org/10.1117/1.3500463.
5. I. Abdulhalim et al., "Surface enhanced fluorescence from metal sculptured thin films with application to biosensing in water," *Appl. Phys. Lett.* **94**(6), 063106 (2009), http://dx.doi.org/10.1063/1.3081031.
6. K. Kneipp et al., "Surface-enhanced Raman scattering: a new tool for biomedical spectroscopy," *Curr. Sci.* **77**, 915–924 (1999).
7. A. Shalabney and I. Abdulhalim, "Electromagnetic fields distribution in multilayer thin film structures and the origin of sensitivity enhancement in surface plasmon resonance sensors," *Sens. Actuator. A Phys.* **159**(1), 24–32 (2010), http://dx.doi.org/10.1016/j.sna.2010.02.005.
8. A. Shalabney and I. Abdulhalim, "Sensitivity-enhancement methods for surface plasmon sensors," *Laser Photon. Rev.* **5**(4), 571–606 (2011), http://dx.doi.org/10.1002/lpor.v5.4.
9. R. Singh, "Why silicon is and will remain the dominant photovoltaic material," *J. Nanophoton.* **3**, 032503 (2009), http://dx.doi.org/10.1117/1.3196882.
10. M. Kerker, D. S. Wang, and H. Chew, "Surface enhanced Raman scattering (SERS) by molecules adsorbed at spherical particles," *Appl. Opt.* **19**(19), 3373–3388 (1980), http://dx.doi.org/10.1364/AO.19.003373.
11. M. Inoue and K. Ohtaka, "Surface enhanced Raman scattering by metal spheres. I. cluster effect," *J. Phys. Soc. Jpn.* **52**(11), 3853–3864 (1983), http://dx.doi.org/10.1143/JPSJ.52.3853.
12. M. Moskovits, "Surface enhanced spectroscopy," *Rev. Mod. Phys.* **57**(3), 783–828 (1985), http://dx.doi.org/10.1103/RevModPhys.57.783.
13. B. Schrader and D. S. Moore, "Laser-based molecular spectroscopy for chemical analysis-Raman scattering processes," *Pure Appl. Chem.* **69**(7), 1451–1468 (1997), http://dx.doi.org/10.1351/pac199769071451.
14. G. C. Schatz and R. P. Van Duyne, "Electromagnetic mechanism of surface-enhanced spectroscopy," Reproduced from: *Handbook of Vibrational Spectroscopy*, J. M.Chalmers and P. R. Griffiths, Eds., John Wiley & Sons Ltd, Chichester (2002).
15. D. Petrov, "Commentary: Raman nanospectroscopy of single DNA molecules," *J. Nanophoton.* **4**, 040306 (2010), http://dx.doi.org/10.1117/1.3515371.
16. C. J. Orendorff et al., "Aspect ratio dependence on surface enhanced Raman scattering using silver and gold nanorod substrates," *Phys. Chem. Chem. Phys.* **8**(1), 165–170 (2006), http://dx.doi.org/10.1039/b512573a.
17. S. N. Lee et al., "Studies of bisphenol-A–polycarbonate aging by Raman difference spectroscopy," *J. Molec. Struct.* **521**(1–3), 19–23 (2000), http://dx.doi.org/10.1016/S0022-2860(99)00422-6.
18. N. Kunapareddy, J. P. Freyer, and J. R. Mourant, "Raman spectroscopic characterization of necrotic cell," *J. Biomed. Opt.* **13**(5), 054002 (2008), http://dx.doi.org/10.1117/1.2978061.
19. M. Kiran et al., "Selective detection of HbA1c using surface enhanced resonance Raman spectroscopy," *Anal. Chem.* **82**(4), 1342–1348 (2010), http://dx.doi.org/10.1021/ac902364h.
20. S. Shanmukh et al., "Rapid and sensitive detection of respiratory virus molecular signatures using a silver nanorod array SERS substrate," *Nano lett.* **6**(11), 2630–2636 (2006), http://dx.doi.org/10.1021/nl061666f.
21. H. Xu et al., "Spectroscopy of single hemoglobin molecules by surface enhanced Raman scattering," *Phys. Rev. Lett.* **83**(21), 4357–4360 (1999), http://dx.doi.org/10.1103/PhysRevLett.83.4357.
22. J. B. Jackson et al., "Controlling the surface enhanced Raman effect via the nanoshell geometry," *Appl. Phys. Lett.* **82**(2), 257–259 (2003), http://dx.doi.org/10.1063/1.1534916.
23. T. Wang, X. Hu, and S. Dong, "Surfactantless synthesis of multiple shapes of gold nanostructures and their shape-dependent SERS spectroscopy," *J. Phys. Chem. B* **110**(34), 16930–16936 (2006), http://dx.doi.org/10.1021/jp062486x.

24. Y. Wang et al., "Effect of silver nanoplates on raman spectra of p-aminothiophenol assembled on smooth macroscopic gold and silver surface," *J. Phys. Chem. C* **111**(8), 3259–3265 (2007), http://dx.doi.org/10.1021/jp066444k.
25. S. A. Kalele et al., "Plasmon-assisted photonics at the nanoscale," *J. Nanophoton.* **1**, 12501 (2007), http://dx.doi.org/10.1117/1.2748429.
26. H. Gai, J. Wang, and Q. Tian, "Tuning the resonant wavelength of a nanometric bow-tie aperture by altering the relative permittivity of the dielectric substrate," *J. Nanophoton.* **1**, 013555 (2007), http://dx.doi.org/10.1117/1.2822393.
27. Q. Zhou et al., "Arrays of aligned, single crystalline silver nanorods for trace amount detection," *J. Phys. D Appl. Phys.* **41**(15), 152007–152010 (2008), http://dx.doi.org/10.1088/0022-3727/41/15/152007.
28. N. Félidj, J. Aubard, and G. Lévi, "Enhanced substrate-induced coupling in two-dimensional gold nanoparticle arrays," *Phys. Rev. B* **66**(24), 245407 (2002), http://dx.doi.org/10.1103/PhysRevB.66.245407.
29. A. Tao et al., "Langmuir-blodgett silver nanowire monolayers for molecular sensing using surface-enhanced Raman spectroscopy," *Nano lett.* **3**(9), 1229–1233 (2003), http://dx.doi.org/10.1021/nl0344209.
30. N. Félidj et al., "Controlling the optical response of regular arrays of gold particles for surface-enhanced Raman scattering," *Phys. Rev. B* **65**(7), 075419 (2002), http://dx.doi.org/10.1103/PhysRevB.65.075419.
31. R. Greenler and T. Slager, "Method for obtaining the Raman spectrum of a thin film on a metal surface," *Spectrochim. Acta* **29**(1), 193–201 (1973), http://dx.doi.org/10.1016/0584-8539(73)80022-4.
32. Y. Liu and Y. Zhao, "Simple model for surface-enhanced Raman scattering from tilted silver nanorod array substrates," *Phys. Rev. B* **78**(7), 075436–075444 (2008), http://dx.doi.org/10.1103/PhysRevB.78.075436.
33. C. L. Leverette et al., "Aligned silver nanorod arrays as substrates for surface-enhanced infrared absorption spectroscopy," *Appl. Spectrosc.* **60**(8), 906–913 (2006), http://dx.doi.org/10.1366/000370206778062084.
34. Y. Liu et al., "Angle dependent surface enhanced Raman scattering obtained from a Ag nanorods array substrate," *Appl. Phys. Lett.* **89**(17), 173134 (2006), http://dx.doi.org/10.1063/1.2369644.
35. Y. P. Zhao et al., "Polarized surface enhanced raman and absorbance spectra of aligned silver nanorod arrays," *J. Phys. Chem. B* **110**(7), 3153–3157 (2006), http://dx.doi.org/10.1021/jp057406o.
36. R. Messier, "The nano-world of thin films," *J. Nanophoton.* **2**, 021995 (2008), http://dx.doi.org/10.1117/1.3000671.
37. A. Shalabney et al., "Surface plasmon resonance from metallic columnar thin films," *Photon Nanostruct. Fundam. Appl.* **7**(4), 176–185 (2009), http://dx.doi.org/10.1016/j.photonics.2009.03.003.
38. I. Abdulhalim et al., "Porosity effect on surface plasmon resonance from metallic sculptured thin films," *Proc. SPIE* **7041**, 70410C (2008), http://dx.doi.org/10.1117/12.794135.
39. I. Abdulhalim et al., "Comparative study of enhanced fluorescence from nano sculptured thin films,," *Proc. SPIE* **7041**, 70410G (2008), http://dx.doi.org/10.1117/12.795139.
40. A. Shalabney et al., "Sensitivity of surface plasmon resonance sensors based on metallic columnar thin films in the spectral and angular interrogation," *Sens. Actuat. B Chem.* **159**(1), 201–212 (2011), http://dx.doi.org/10.1016/j.snb.2011.06.072.
41. M. Suzuki et al., "Ag nanorod arrays tailored for surface-enhanced Raman imaging in the near-infrared region," *Nanotechnology* **19**(26), 265304 (2008), http://dx.doi.org/10.1088/0957-4484/19/26/265304.
42. M. Suzuki et al., "Au nanorod arrays tailored for surface-enhanced Raman spectroscopy," *Anal. Sci.* **23**(7), 829–833 (2007), http://dx.doi.org/10.2116/analsci.23.829.
43. M. Suzuki et al., "In-line aligned and bottom-up Ag nanorods for surface-enhanced Raman spectroscopy," *Appl. Phys. Lett.* **88**(20), 203121 (2006), http://dx.doi.org/10.1063/1.2205149.

44. M. Suzuki et al., "Tailoring coupling of light to local plasmons by using Ag nanorods/structured dielectric/mirror sandwiches," *J. Nanophoton.* **3**, 031502 (2009), http://dx.doi.org/10.1117/1.3079804.
45. R. Messier and A. Lakhtakia, "Sculptured thin films—II. Experiments and applications," *Mater. Res. Innovat.* **2**(4), 217–222 (1999), http://dx.doi.org/10.1007/s100190050088.
46. F. Tang et al., "Unusual magnesium crystalline nanoblades grown by oblique angle vapor deposition," *J. Nanosci. Nanotechnol.* **7**(9), 3239–3244 (2007), http://dx.doi.org/10.1166/jnn.2007.665.
47. E. Schubert et al., "Nanostructure fabrication by glancing angle ion beam assisted deposition of silicon," *Appl. Phys. A* **81**(3), 481–486 (2005), http://dx.doi.org/10.1007/s00339-005-3270-9.
48. C. Patzig et al., "Ordered silicon nanostructures by ion beam induced glancing angle deposition," *J. Vac. Sci. Technol. B* **25**(3), 833–838 (2007), http://dx.doi.org/10.1116/1.2737436.
49. B. Fuhrmann, H. Leipner, and H. Höche, "Ordered arrays of silicon nanowires produced by nanosphere lithography and molecular beam epitaxy," *Nano Lett.* **5**(12), 2524–2527 (2005), http://dx.doi.org/10.1021/nl051856a.
50. L. Jiao et al., "Simple azo derivatization on 4-aminothiophenol/Au monolayer," *Electrochem. Commun.* **7**(2), 219–222 (2005), http://dx.doi.org/10.1016/j.elecom.2004.12.014.
51. E. C. Le Ru et al., "Surface enhanced Raman scattering enhancement factors: a comprehensive study," *J. Phys. Chem. C* **111**(37), 13794–13803 (2007), http://dx.doi.org/10.1021/jp0687908.
52. X. Hu et al., "Surface-enhanced raman scattering of 4-aminothiophenol self-assembled monolayers in sandwich structure with nanoparticle shape dependence: off-surface plasmon resonance condition," *J. Phys. Chem. C* **111**(19), 6962–6969 (2007), http://dx.doi.org/10.1021/jp0712194.
53. K. Kim and J. Yoon, "Raman scattering of 4-aminobenzenethiol sandwiched between Ag/Au nanoparticle and macroscopically smooth Au substrate," *J. Phys. Chem. B* **109**(40), 18929 (2005), http://dx.doi.org/10.1021/jp052665z.
54. M. G. Banaee and K. B. Crozier, "Gold nanorings as substrates for surface-enhanced Raman scattering," *Opt. Lett.* **35**(5) (2010), http://dx.doi.org/10.1364/OL.35.000760.
55. P. Camargo et al., "Measuring the SERS enhancement factors of dimers with different structures constructed from silver nanocubes," *Chem. Phys. Lett.* **484**(4–6), 304–308 (2010), http://dx.doi.org/10.1016/j.cplett.2009.12.002.
56. J. Zheng et al., "Surface-enhanced raman scattering of 4-aminothiophenol in assemblies of nanosized particles and the macroscopic surface of silver," *Langmuir* **19**(3), 632–636 (2003), http://dx.doi.org/10.1021/la011706p.
57. S. K. Saikin et al., "Separation of electromagnetic and chemical contributions to surface-enhanced Raman spectra on nanoengineered plasmonic substrates," *J. Phys. Chem. Lett.* **1**(18), 2740–2746 (2010), http://dx.doi.org/10.1021/jz1008714.
58. A. Otto, "Surface-enhanced raman scattering of adsorbates," *J. Raman Spectrosc.* **22**(12), 743–752 (1991), http://dx.doi.org/10.1002/jrs.v22:12.
59. K. Uetsuki et al., "Experimental identification of chemical effects in surface enhanced raman scattering of 4-aminothiophenol," *J. Phys. Chem. C* **114**(16), 7515–7520 (2010), http://dx.doi.org/10.1021/jp9114805.
60. K. Yoshida et al., "Quantitative evaluation of electromagnetic enhancement in surface-enhanced resonance Raman scattering from plasmonic properties and morphologies of individual Ag nanostructures," *Phys. Rev. B* **81**(11), 115406–115414 (2010), http://dx.doi.org/10.1103/PhysRevB.81.115406.
61. K. Imura et al., "Visualization of localized intense optical fields in single gold-nanoparticle assemblies and ultrasensitive raman active sites," *Nano lett.* **6**(10), 2173–2176 (2006), http://dx.doi.org/10.1021/nl061650p.
62. W. Yang, G. Schatz, and R. Van Duyne, "Discrete dipole approximation for calculating extinction and Raman intensities for small particles with arbitrary shapes," *J. Chem. Phys.* **103**(3), 869–875 (1995), http://dx.doi.org/10.1063/1.469787.

63. R. Boyack and E. Le Ru, "Investigation of particle shape and size effects in SERS using T-matrix calculations," *Phys. Chem. Chem. Phys.* **11**(34), 7398–7405 (2009), http://dx.doi.org/10.1039/b905645a.
64. H. Kuwata et al., "Resonant light scattering from metal nanoparticles: practical analysis beyond Rayleigh approximation," *Appl. Phys. Lett.* **83**(22), 4625–4627 (2003), http://dx.doi.org/10.1063/1.1630351.
65. C. Geddes et al., "Silver fractal-like structures for metal-enhanced flourescence: enhanced flourescence intensitites and increased probe photostabilities," *J. Flouresc.* **13**(3), 267–276 (2003), http://dx.doi.org/10.1023/A:1025046101335.
66. J. Lakowicz et al., "Advances in surface-enhanced fluorescence," *J. Fluoresc.* **14**(4), 425–441 (2004), http://dx.doi.org/10.1023/B:JOFL.0000031824.48401.5c.
67. G. Schatz, "Theoretical studies of surface enhanced Raman scattering," *Acc. Chem. Res.* **17**(10), 370–376 (1984), http://dx.doi.org/10.1021/ar00106a005.
68. E. C. Stoner, "The demagnetizing factors for ellipsoids," *Philosoph. Mag. Series 7*, **36**(236), 803–812 (1945).
69. W. Wokaun, J. P. Gordon, and P. F. Liau, "Radiation damping in surface enhanced Raman scattering," *Phy. Rev. Lett.* **48**(14), 957–960 (1982), http://dx.doi.org/10.1103/PhysRevLett.48.957.
70. U. Kreibig, "Electronic properties of small silver particles: the optical constants and their temperature dependence," *J. Phys. F Metal Phys.* **4**(7), 999–1014 (1974), http://dx.doi.org/10.1088/0305-4608/4/7/007.
71. W. Kraus and G. Schatz, "Plasmon broadening in spheroidal metal particles," *Chem. Phys. Lett.* **99**(4), 353–357 (1983), http://dx.doi.org/10.1016/0009-2614(83)87555-1.

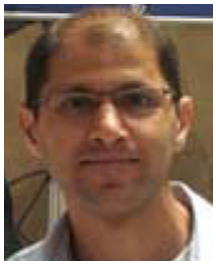

Atef Shalabney received his bachelor of sciences in electrical engineering from the Technion, Institute of Technology, Hafia, Israel, in 1997, and a master degree in electro-optics engineering from the Ben Gurion University, Beer Shiva, Israel, in 2009. Currently, he is a PhD student in electro-optics engineering at Ben Gurion University. His research interests are plasmonic structures and optical biosensing devices.

Chinmay Khare obtained his PhD in physics from the BuildMoNa Graduate School, Universität Leipzig under supervision of Prof. Dr. B. Rauschenbach at Leibniz Institute of Surface Modification, Leipzig. His research interests focus on synthesis and characterization of glancing angle deposited nanostructures. In January 2012, he joined Ruhr-Universität Bochum, Germany as a post-doc.

Jens Bauer studied physics at the University of Leipzig, Germany. He carried out his PhD in the semiconductor chemistry group in the department of inorganic chemistry at the University of Leipzig, where he investigated the epitaxial growth of single crystalline III-V nanowires. Since 2009, he has been working at the Leibniz-Institute of surface science (IOM) in Leipzig, Germany. His research interests cover the physical deposition and structural characterization of metallic and semiconductor nanostructured thin films.

Bernd Rauschenbach is the director of the Leibniz Institute of Surface Modification (IOM) and professor of Applied Physics at the University Leipzig (Germany). His fields of research are the interaction of ion and laser beams with solid surfaces, the nanotechnology, and the prepararion and characterization of thin films. (photograph not available)

Ibrahim Abdulhalim is a professor and head of the Department of Electro-optic Engineering at Ben Gurion University. He has worked in academic institutions and companies such as the OCSC in UC at Boulder, the ORC at Southampton University, the Thin Films Center of the University of Western Scotland, in KLA-Tencor, Nova and GWS Photonics. His current research involve: LC devices, Plasmonics for biosensing, biomedical optical imaging techniques. Published over 160 articles, one book, and 10 patents. He is a fellow of IoP and SPIE and an associate editor for the *Journal of Nanophotonics* and for *Physics Express*.